

Article

The Vertical Distributions of Aerosol Optical Characteristics Based on Lidar in Nanyang City from 2021 to 2022

Miao Zhang ^{1,2,3,*} , Si Guo ¹, Yunuo Wang ¹, Shiyong Chen ¹, Jinhan Chen ¹, Mingchun Chen ⁴ and Muhammad Bilal ^{5,*} 

¹ Academy of Remote Sensing Technology and Application, Nanyang Normal University, Wolong Road No. 1638, Nanyang 473061, China

² Key Laboratory of Natural Disaster and Remote Sensing of Henan Province, Nanyang Normal University, Wolong Road No. 1638, Nanyang 473061, China

³ Engineering Research Center of Environmental Laser Remote Sensing Technology and Application of Henan Province, Nanyang Normal University, Wolong Road No. 1638, Nanyang 473061, China

⁴ Teacher Education College, Beijing Language and Culture University, Xueyuan Road No. 15, Beijing 100083, China

⁵ School of Surveying and Land Information Engineering, Henan Polytechnic University, Jiaozuo 454000, China

* Correspondence: zm_liesmars@whu.edu.cn (M.Z.); muhammad.bilal@connect.polyu.hk (M.B.); Tel.: +86-151-3909-7793 (M.Z.)

Abstract: To investigate the vertical distribution of aerosol optical characteristics in Nanyang City, a ground-based dual-wavelength (532 nm and 355 nm) lidar system was developed for aerosol observation at the Nanyang Normal University Station (NYNU) from November 2021 to December 2022. Spatio-temporal dynamics information on vertical distributions of aerosol optical properties during polluted and non-polluted days was obtained. Aerosols were characterized by low altitudes (up to 2 km), thinner layers, and high-altitude (up to 4 km) thick layers during non-polluted and polluted days, with extinction coefficient values of $\sim 0.03 \text{ km}^{-1}$ and $\sim 0.2 \text{ km}^{-1}$, respectively. The mean values of the extinction coefficient at different altitudes (0~5 km) were all about ten-times higher on polluted days ($0.04\sim 0.19 \text{ km}^{-1}$) than on non-polluted days ($0.004\sim 0.02 \text{ km}^{-1}$). These results indicate that aerosol loadings and variations at different altitudes (0~5 km) were much higher and more prominent on polluted days than non-polluted days. The results show ten-times larger aerosol optical depth (AOD) values ($0.4\sim 0.6$) on polluted days than on non-polluted days ($0.05\sim 0.08$). At the same time, AOD values on both polluted and non-polluted days slightly decreased from 19:00 to 05:00, possibly due to dry depositions at nighttime. For the first time, this study established a ground-based lidar remote sensing system to investigate the vertical distribution of atmospheric aerosol optical characteristics in Henan Province. The experimental results can provide scientific dataset support for the local government to prevent and control air pollution.

Keywords: aerosol; particle; lidar; vertical distribution; optical property



Citation: Zhang, M.; Guo, S.; Wang, Y.; Chen, S.; Chen, J.; Chen, M.; Bilal, M. The Vertical Distributions of Aerosol Optical Characteristics Based on Lidar in Nanyang City from 2021 to 2022. *Atmosphere* **2023**, *14*, 894. <https://doi.org/10.3390/atmos14050894/>

Academic Editor: Alexandros Papayannis

Received: 10 April 2023

Revised: 10 May 2023

Accepted: 17 May 2023

Published: 20 May 2023



Copyright: © 2023 by the authors. Licensee MDPI, Basel, Switzerland. This article is an open access article distributed under the terms and conditions of the Creative Commons Attribution (CC BY) license (<https://creativecommons.org/licenses/by/4.0/>).

1. Introduction

Aerosols are solid or liquid particles suspended in the atmosphere, ranging from submicron to 100s of microns [1,2]. Aerosols can absorb or scatter solar radiation, thus affecting the earth's radiation balance, or act as condensation nuclei of clouds, altering their life cycles and affecting the climate system [3–9]. With the increasing mass concentration of suspended particulate matter in the atmosphere, haze pollution events could occur [10,11], deteriorating visibility and air quality [12–16]. Therefore, an observational study of the aerosol is a prerequisite for haze management and is of great scientific importance [17–21].

The vertical aerosol distribution is essential information for studying aerosol characteristics, which can influence weather and climate change. The vertical distribution of aerosols changes rapidly, bringing some uncertainty to aerosol monitoring [22–24]. Traditional aerosol observation techniques, such as station sampling observation, can only

obtain information about the aerosol near the surface but not the vertical distribution of the aerosols. Accurate acquisition of spatial three-dimensional vertical dynamic details of the aerosol layer is necessary and will improve the accuracy of aerosol monitoring and traceability. Lidar remote sensing technology has a high temporal resolution, which has been gradually applied to obtain aerosol vertical distributions [25–30]. By actively emitting laser signals and receiving the scattering signals of atmospheric aerosol and molecules, Lidar can accurately obtain the vertical distribution of aerosol optical characteristics and provide the necessary means for atmosphere research [31–34].

Many researchers worldwide have studied aerosols' vertical distribution using Lidar remote sensing technology and have achieved remarkable results [19,26,35–38]. Sicard et al., developed and tested a dual-wavelength lidar system based on 1064 and 532 nm to observe aerosols vertically [39]. Gasmi et al., used a home-built ground-based Lidar system to achieve aerosol/cloud profiles in the lower atmosphere [40]. Liu et al., developed a dual-field Lidar system, which enabled the simultaneous acquisition of near- and far-field aerosol data, effectively improving the detection altitude range of the Lidar system [41]. Li et al., developed an integrated fluorescence-Mie Lidar to achieve fluorescence aerosol profile information in meteorological monitoring [42]. Shukla et al., studied the vertical distribution of the aerosol layer over the Himalayas using the range correction signal of micro-pulse Lidar [43]. Zhu et al., compared the difference in vertical aerosol distribution between urban and suburban areas and studied the influence of regional transport on local pollution sources [44]. Sugimoto et al., studied the vertical distribution of the extinction coefficient and depolarization ratio of aerosols utilizing the Mie–Raman polarization Lidar in Phimai, Thailand [45]. Rosati et al., also studied the vertical distribution of extinction coefficients of aerosols in the atmospheric boundary layer at the San Pietro Capofiume (SPC) station in Italy using an elastic scattering Lidar [46]. Based on Lidar's advantages in atmospheric observation, the Lidar aerosol European observation network (EARLINET) was established worldwide, which played an essential role in global aerosol profile acquisition and application [47,48]. In summary, Lidar technology, with a wide range of detection altitudes and strong data signal-to-noise ratio, is essential for aerosol observation.

In this study, we developed a ground-based dual-wavelength (532 nm and 355 nm) Lidar system for aerosol observation. The experimental site was chosen in the Nanyang Normal University (NYNU) station in Nanyang City, Henan Province, China. The study period was from November 2021 to December 2022. Information on vertical aerosol distribution in hazy and clear weather was obtained, which can provide scientific data support and theoretical support for haze prevention and control in Nanyang City. According to previous reports, no relevant team in Henan Province has been found to develop ground-based Lidar in haze experimental observation. Additionally, this experiment is the first to establish a ground-based Lidar system and utilize it to observe the vertical distribution of atmospheric aerosol optical characteristics in Henan Province. The experimental site, equipment, and research methods are explained in Section 2, the results and discussion are presented in Section 3, and the conclusion is in Section 4.

2. Materials and Methods

2.1. Experimental Site

The NYNU site (32°58' N, 112°29' E) is located in Nanyang City, Henan Province, China (Figure 1). Nanyang City borders Hubei Province and Shanxi Province, which is the core city of the central Plains economic zone and the sub-center city of Henan Province. Nanyang belongs to China's typical subtropical continental monsoonal climate and the Yangtze River basin. Nanyang has four distinct seasons and moderate annual precipitation (1295.8 mm), and a yearly temperature of 16.7 °C [49]. It is located north of the Funiu Mountains and the Han River. It is the largest prefecture-level city in Henan Province, with an area of 26,600 square kilometers and a population of 9,629,000. Nanyang has a privileged geographical position, convenient transportation, and well-developed transportation. In recent years, Nanyang has become an emerging regional economic center

and a national comprehensive transportation hub. This rapid economic development has been accompanied through frequently increasing serious haze pollution events, making it imperative to monitor and study the haze in Nanyang.

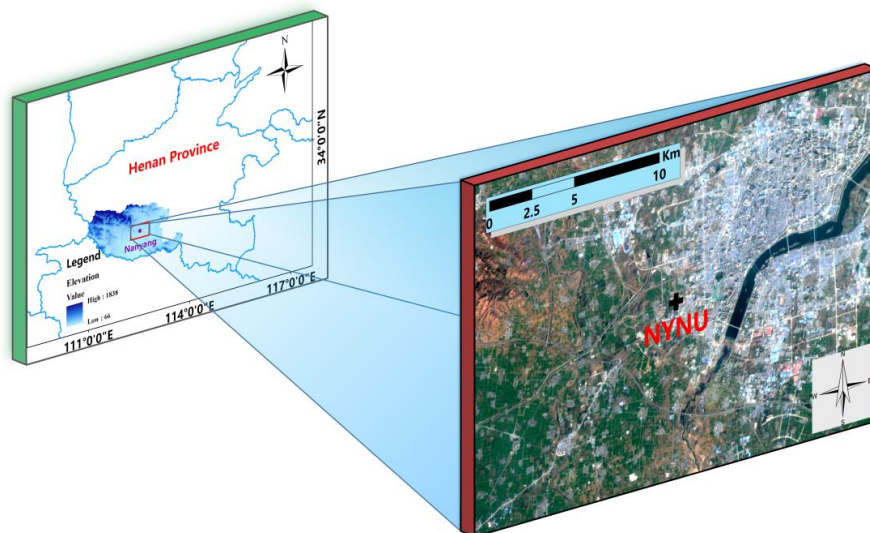


Figure 1. The location information of the experimental site.

2.2. Lidar Equipment

The 2-wavelength Lidar system consists of a laser transmitting system, an optical telescope receiving system, and a signal acquisition processing system. Figure 2 shows a schematic diagram of the Lidar, and Table 1 gives the technical parameters of the system. The laser transmitting and the optical telescope receiving systems (high-power pulsed laser, transmission unit, laser power meter, laser echo spectroscopy detector, telescope, photomultiplier tube) are placed on an optical platform for long time series of stable observations. The signal acquisition system (IPC, mobile data acquisition controller, echo signal monitor) is housed in the PDU acquisition cabinet. As shown in Figure 2, the transmission unit consists of three parts (total reflector 1, collimated beam expander 2, and total reflector 3). The laser beam from the high-power pulsed laser is passed through the total reflector 1 and then directed through the collimating beam expander 2, where the beam diameter changes from 1 cm to 3 cm, and then to the total reflector 3. By adjusting the angle of the total reflector 3, the final output laser beam is parallel to the receiving telescope's optical axis. It is directed vertically into the sky through the skylight at the top of the laboratory (Figure 3).

After the two telescopes had picked up all the received light, the visible 532 nm signal was filtered out by green filter 4 and picked up by the telescope (MEADE LX200), and the 355 nm signal was filtered out by UV filter 5 and picked up by the telescope (MEADE LX850). Then, signals of the two channels were concentrated in their respective photomultiplier tubes. The signal of each channel is amplified by a signal amplifier behind the photomultiplier, which is then used for analog-to-digital conversion and acquisition via the digital acquisition card.

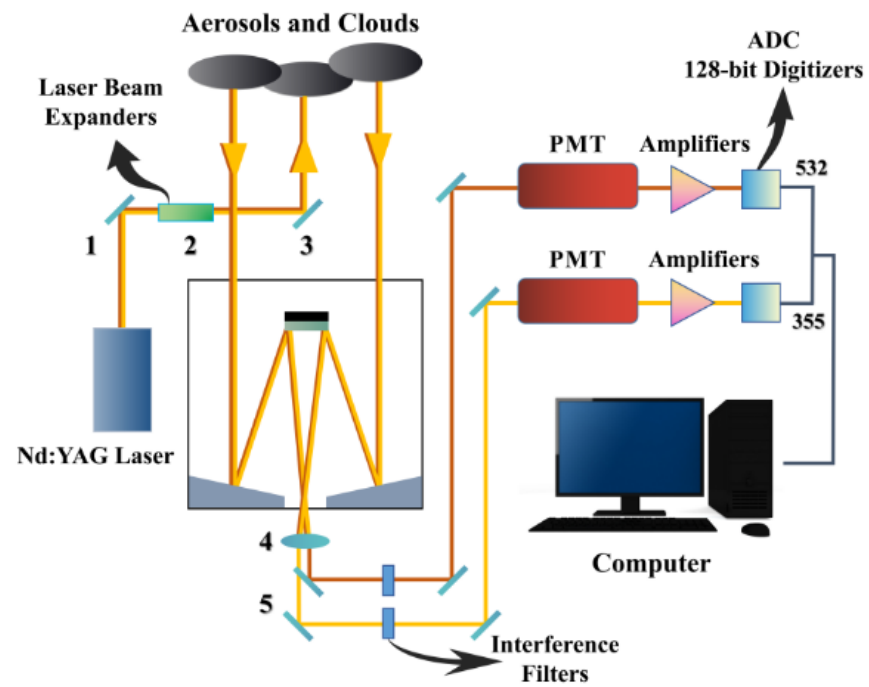


Figure 2. Schematic diagram of the 2-wavelength Lidar system.

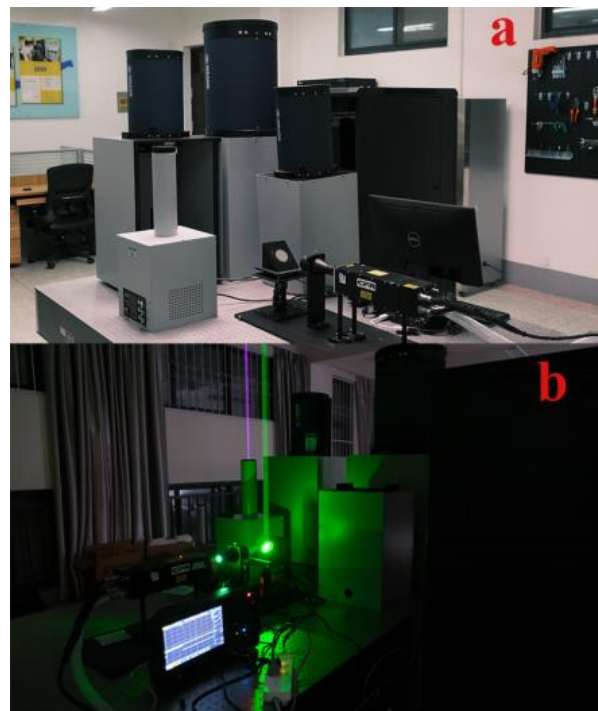


Figure 3. The 2-wavelength Lidar system at the NYNU site: (a) the 2-wavelength Lidar device in non-operation; (b) the 2-wavelength Lidar equipment in operation.

Table 1. Equipment parameters of the 2-wavelength Lidar system.

Laser emission systems	
Lasers	Quantel CFR BIG SKY Q-switched Nd: YAG
Wavelength	532 nm, 355 nm
Pulse energy	130 mJ@532 nm, 60 mJ@355 nm
Maximum heavy frequency	20 Hz
Pulse width	10 ns@532 nm, 9 ns@355 nm
angle of divergence	0.25 mrad
Optical reception systems	
Model	MEADE Schmidt-Cassegrain (MEADE LX200/MEADE LX850)
Focal length	2000 mm/4064 mm
Calibre	203 mm (8 in)/355 mm (14 in)
Field of view	1.5 mrad (Adjustable)
Filter bandwidth	3 nm
Signal acquisition systems	
High resolution	7.68 m
Time resolution	Adjustable (common 60 s)
Data processing	Automated, Manual
Sampling rate	50 ns

2.3. Experimental Methodology

The Lidar emits laser pulses vertically into the sky. The scattering occurs when the laser pulses hit the atmospheric particles and molecules, where the backscattered signal returns vertically to the receiving telescope. The profiles of aerosol optical properties (extinction coefficient, backscattering coefficient) can be obtained by inversion of the backscattering signals. After the Lidar receives the echo signal of atmospheric aerosol particles and molecules, it is necessary to retrieve it to obtain accurate aerosol optical properties quantitatively. Several researchers have contributed to this area by proposing many Lidar aerosol retrieval algorithms. For example, Collis et al., proposed the slope method based on homogeneous aerosols [50], Klett et al., proposed the aerosol composition method [51], and Fernald et al., proposed the inversion method considering molecules and aerosols [52]. The slope method is premised on the assumption that the aerosols in the atmospheric environment are uniformly distributed and that the backscattering and extinction coefficients in the inversion equations are constants; the Klett–Fernald inversion method is currently the classical method for retrieving aerosol extinction coefficient profiles from Lidar signals. In this method, if the extinction coefficients of aerosol particles and atmospheric molecules at a certain altitude z_i are known in advance, the backscattering and extinction coefficients of aerosol particles at altitudes above the reference altitude z_i can be obtained by using the Fernald forward integration method. Similarly, the backscattering and extinction coefficients of aerosol particles at each height below the reference height z_i can also be found using the Fernald backward integration method. The relevant formula is shown as follows:

Backward integration:

$$\beta_a(i-1) = \frac{X(i-1) \exp[A(i-1)]}{\frac{X(i)}{\beta_a(i)} + S_a\{X(i) + X(i-1)\exp[A(i-1)]\}\Delta z} - \beta_m(i-1) \quad (1)$$

Forward integration:

$$\beta_a(i+1) = \frac{X(i+1) \exp[-A(i)]}{\frac{X(i)}{\beta_a(i)} - S_a\{X(i) + X(i+1)\exp[-A(i)]\}\Delta z} - \beta_m(i+1) \quad (2)$$

where β_a is the backscattering coefficient of aerosol particles, $X(z) = P(z)z^2$, and the subscripts a and m denote aerosol particles and atmospheric molecules, respectively. S_a and S_m are the Lidar ratios of aerosol and atmospheric molecules. In this method, three parameters must be assumed [52]: (1) The Lidar ratio S_a is chosen roughly depending on the prevailing aerosol type/size. A value of 50 sr is often preferred for unknown or mixed aerosols. This study assumes S_a as a fixed constant value of 50 Sr in the 532 nm band. S_m is supposed to be $8\pi/3$ Sr [53–56]. (2) The backscattering coefficient of atmospheric molecules β_m is derived using the U.S. Standard Atmosphere Model and Rayleigh scattering theory [51,52]. (3) The boundary value $X(i)$ is solved via the matching method assuming the existence of a clean atmosphere at the top of the troposphere (at a determined height z_i), where the aerosol backscattering ratio is usually considered to be $\beta_a(z_i)/\beta_m(z_i) = 0.02$ [51,52].

In this experiment, we only use 532 nm data for analysis; the variables include 532 nm extinction coefficient profile data and 532 nm AOD data. Because of the intense sunlight and the poor signal-to-noise ratio during the daytime, all the experimental observations were carried out at night. This study divided the data into polluted and pollution-free weather and compared the vertical distribution of aerosol extinction coefficients. According to the standard of $PM_{2.5}$ data of Nanyang Meteorological Bureau, the weather with a daily average of $PM_{2.5}$ mass concentration greater than $75 \mu\text{g}/\text{m}^3$ was regarded as pollution weather, and the weather in which a daily average of $PM_{2.5}$ mass concentration less than $75 \mu\text{g}/\text{m}^3$ was considered as pollution-free weather. This rule was consistent with the Chinese ambient air quality standards (secondary quality standard, $75 \mu\text{g}/\text{m}^3$ 24 h average of $PM_{2.5}$) [57]. The time used in this study was the local time (L.T.).

3. Results and Discussion

3.1. Lidar-Based Vertical Distribution of Pollution-Free Weather Aerosols in Nanyang

Figure 4 displays the altitude-time color map of 2-wavelength Lidar for pollution-free weather at the NYNU site. Meanwhile, Table 2 displays the statistical information of mean values, standard deviations, and percentiles of extinction coefficients at various heights during the pollution-free period. It can be seen that average values of the extinction coefficients at 1 km, 2 km, and 3 km altitudes were 0.0221 km^{-1} , 0.0234 km^{-1} , and 0.0114 km^{-1} during pollution-free weather, respectively, while the values of the extinction coefficients above 4 km were all less than 0.01 km^{-1} , indicating that aerosols were mainly concentrated below 3 km. The standard deviation values of the extinction coefficients at 1 km, 2 km, and 3 km heights were 0.0068, 0.0052, and 0.0033 during pollution-free weather, respectively, while the values of standard deviation above 4 km were all less than 0.003, indicating that aerosol extinction coefficients changed relatively more significantly below 3 km than above 3 km.

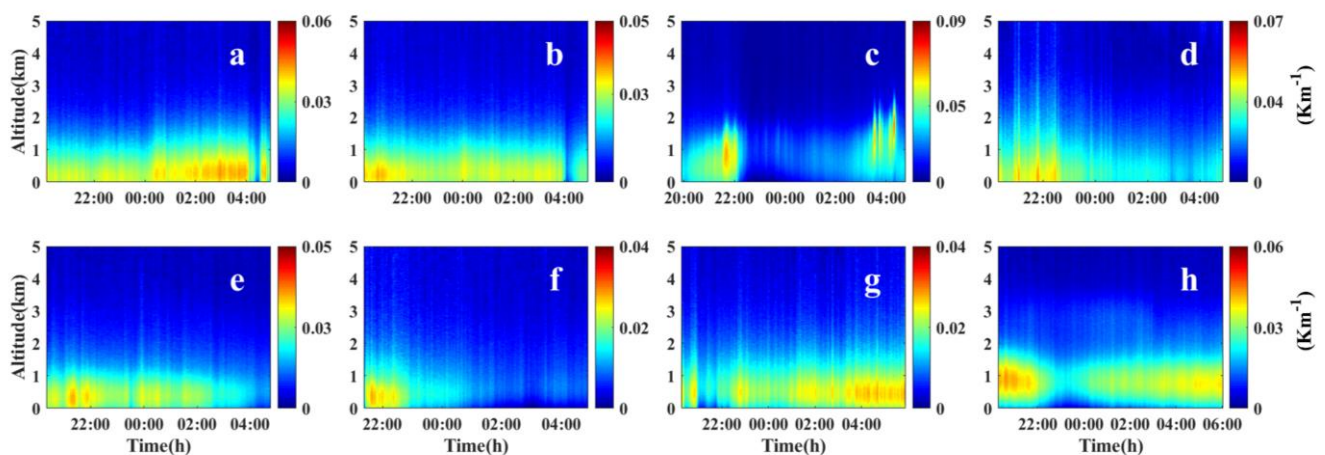


Figure 4. Altitude-time color map of 2-wavelength Lidar for pollution-free weather at NYNU site: (a) 4 May 2022; (b) 5 May 2022; (c) 6 May 2022; (d) 15 May 2022; (e) 20 May 2022; (f) 22 May 2022; (g) 11 October 2022; (h) 17 October 2022.

Table 2. Extinction coefficients at various heights during the pollution-free period.

R (km)	Mean (km ⁻¹)	S.D.	P (km ⁻¹)					
			10%	25%	50%	75%	90%	
0	0.0001	0.0001	0.0000	0.0001	0.0001	0.0001	0.0001	0.0001
1	0.0221	0.0068	0.0138	0.0177	0.0222	0.0264	0.0307	0.0307
2	0.0234	0.0052	0.0175	0.0198	0.0225	0.0268	0.0302	0.0302
3	0.0114	0.0033	0.0083	0.0093	0.0107	0.0126	0.0147	0.0147
4	0.0064	0.0021	0.0045	0.0051	0.0060	0.0072	0.0085	0.0085
5	0.0043	0.0018	0.0028	0.0033	0.0040	0.0049	0.0058	0.0058

Figure 5 showed the 532 nm aerosol optical depth (AOD) of the Lidar at the NYNU site in pollution-free weather. Meanwhile, Table 3 displayed AOD statistics information (mean values, standard deviations, percentiles) at various times during the study in pollution-free weather. It can be revealed that mean AOD values of pollution-free weather at the NYNU site were low (0.05~0.08) and showed a decreasing trend from 19:00 to 5:00 L.T., which could be due to the dry deposition phenomenon of aerosols at night, resulting in a decrease in aerosol concentration after midnight.

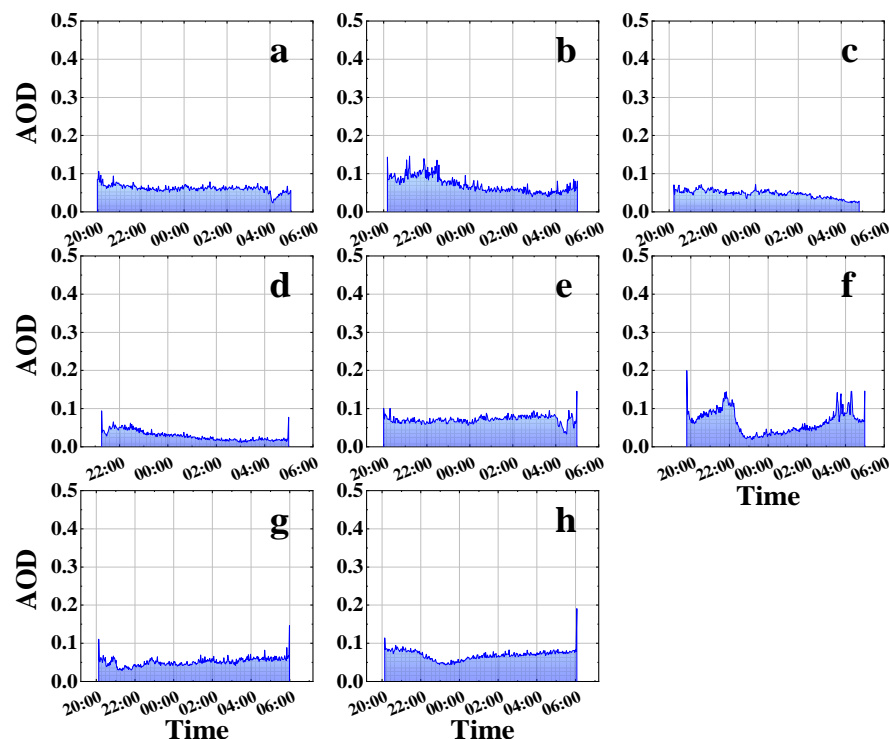


Figure 5. Aerosol 532 nm aerosol optical depth (AOD) of Lidar in NYNU site at pollution-free weather: (a) 4 May 2022; (b) 5 May 2022; (c) 6 May 2022; (d) 15 May 2022; (e) 20 May 2022; (f) 22 May 2022; (g) 11 October 2022; (h) 17 October 2022.

Table 3. AOD statistics at various times during the study in pollution-free weather.

Time	Mean	SD	P				
			10%	25%	50%	75%	90%
19:00	0.076	0.023	0.063	0.063	0.064	0.084	0.095
20:00	0.072	0.013	0.056	0.063	0.074	0.081	0.086
21:00	0.071	0.025	0.044	0.055	0.067	0.086	0.105
22:00	0.061	0.015	0.048	0.051	0.059	0.062	0.075
23:00	0.051	0.015	0.032	0.044	0.049	0.062	0.069
00:00	0.052	0.015	0.034	0.043	0.056	0.062	0.065
01:00	0.054	0.016	0.039	0.047	0.056	0.064	0.069
02:00	0.054	0.019	0.035	0.050	0.054	0.064	0.073

Table 3. Cont.

Time	Mean	SD	P				
			10%	25%	50%	75%	90%
03:00	0.057	0.023	0.030	0.046	0.059	0.073	0.082
04:00	0.055	0.023	0.025	0.040	0.059	0.067	0.079
05:00	0.062	0.015	0.050	0.055	0.063	0.070	0.074

3.2. LIDAR-Based Vertical Distribution of Polluted Weather Aerosols

Figure 6 displays the altitude–time color map of 2-wavelength Lidar for polluted weather at the NYNU site. Meanwhile, Table 4 displays the statistical information of mean values, standard deviations, and percentiles of extinction coefficients at various heights during the polluted period. As shown, during the polluted weather, the mean values of extinction coefficients at 1 km, 2 km, and 3 km heights were 0.1911 km^{-1} , 0.1349 km^{-1} , and 0.0955 km^{-1} , respectively. The mean values of extinction coefficients above 3 km were less than 0.09 km^{-1} , indicating that aerosols were mainly concentrated below 3 km.

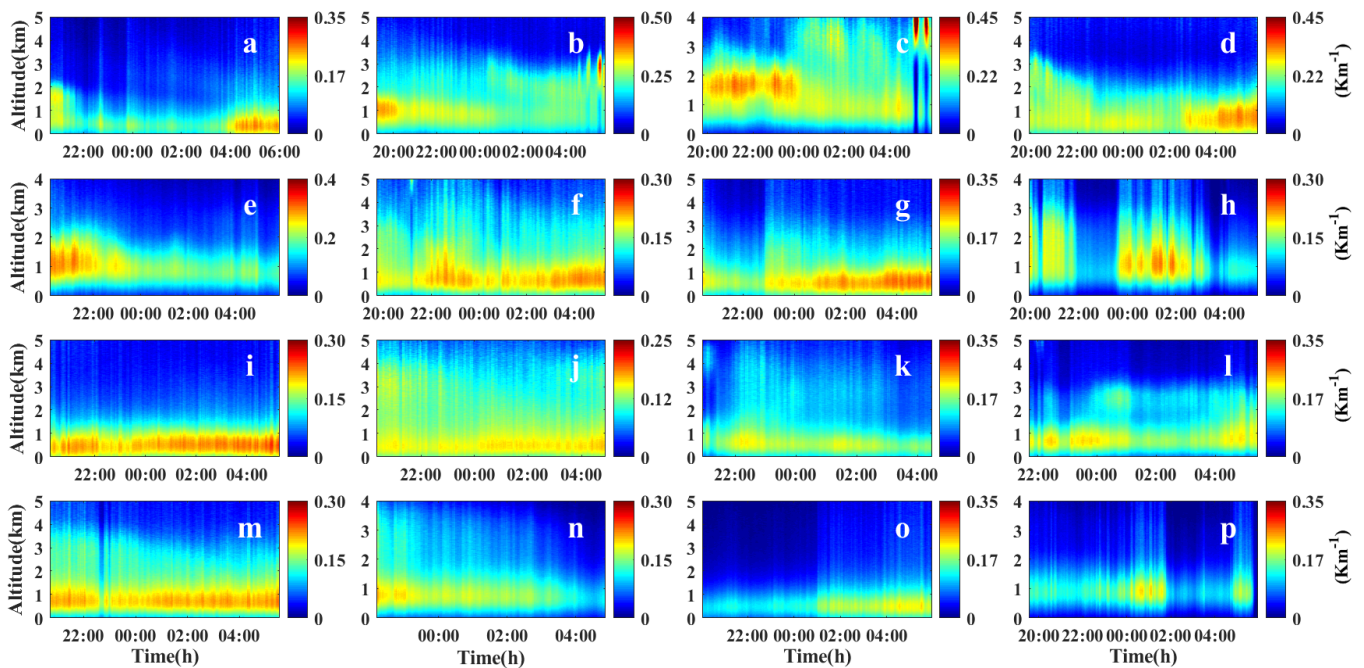


Figure 6. Altitude–time color map of 2–wavelength Lidar for pollution weather in NYNU site: (a) 12 March 2022; (b) 14 March 2022; (c) 1 April 2022; (d) 2 April 2022; (e) 3 April 2022; (f) 9 April 2022; (g) 10 April 2022; (h) 19 April 2022; (i) 21 April 2022; (j) 2 May 2022; (k) 8 June 2022; (l) 2 September 2022; (m) 5 September 2022; (n) 6 September 2022; (o) 10 October 2022; (p) 14 November 2022.

Table 4. Extinction coefficients at various heights during polluted weather.

R (km)	Mean	SD	P				
			10%	25%	50%	75%	90%
0	0.0330	0.0208	0.0215	0.0257	0.0325	0.0381	0.0438
1	0.1911	0.0422	0.1607	0.1755	0.1923	0.2122	0.2281
2	0.1349	0.0413	0.1040	0.1177	0.1335	0.1551	0.1723
3	0.0955	0.0352	0.0663	0.0784	0.0941	0.1114	0.1317
4	0.0622	0.0285	0.0374	0.0451	0.0592	0.0755	0.0908
5	0.0427	0.0202	0.0244	0.0302	0.0401	0.0529	0.0643

Figure 7 shows the 532 nm aerosol optical depth (AOD) of Lidar at the NYNU site in polluted weather. Meanwhile, Table 5 displays AOD statistics information (mean values, standard deviations, percentiles) at various times during the study in pollution-free weather. As shown, the mean values were larger (0.40–0.50) than during the non-polluted period (Table 3). The decreasing trend could be due to the dry deposition of aerosols at night, which led to a decrease in aerosol concentrations after midnight. In summary, AOD values were higher during the polluted winter and spring seasons in Nanyang.

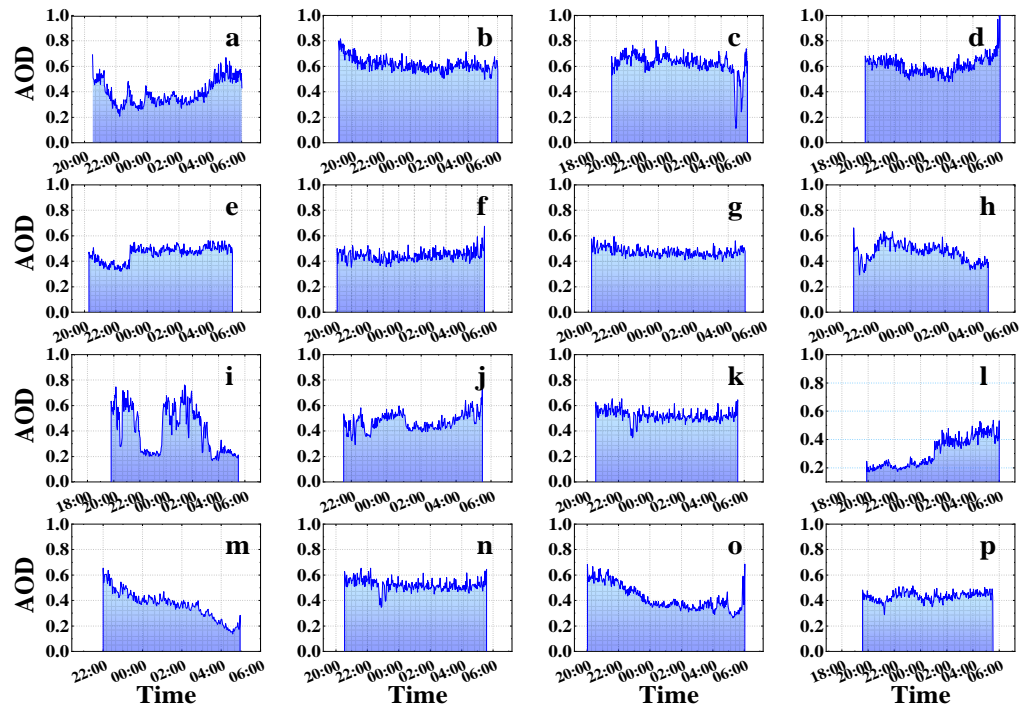


Figure 7. Aerosol 532 nm aerosol optical depth (AOD) of Lidar in NYNU site in pollution weather: (a) 12 March 2022; (b) 14 March 2022; (c) 1 April 2022; (d) 2 April 2022; (e) 3 April 2022; (f) 9 April 2022; (g) 10 April 2022; (h) 19 April 2022; (i) 21 April 2022; (j) 2 May 2022; (k) 8 June 2022; (l) 2 September 2022; (m) 5 September 2022; (n) 6 September 2022; (o) 10 October 2022; (p) 14 November 2022.

Table 5. AOD statistics at various times during the study in pollution weather.

Time	Mean	SD	P				
			10%	25%	50%	75%	90%
19:00	0.503	0.188	0.275	0.382	0.581	0.628	0.679
20:00	0.499	0.132	0.337	0.437	0.518	0.580	0.640
21:00	0.471	0.134	0.306	0.401	0.449	0.566	0.637
22:00	0.446	0.133	0.266	0.356	0.470	0.530	0.609
23:00	0.452	0.117	0.312	0.401	0.457	0.520	0.580
00:00	0.463	0.102	0.353	0.402	0.472	0.532	0.578
01:00	0.471	0.089	0.369	0.398	0.454	0.523	0.591
02:00	0.439	0.109	0.335	0.378	0.453	0.482	0.573
03:00	0.431	0.125	0.260	0.379	0.450	0.500	0.606
04:00	0.449	0.134	0.246	0.380	0.467	0.520	0.599
05:00	0.458	0.142	0.262	0.351	0.501	0.544	0.580

3.3. Synthesis of the Measurements

We calculated the mean and standard deviation of extinction coefficient profiles for polluted and non-polluted weather. As shown in Figure 8, it could be seen that the mean value of aerosol extinction coefficient mean values in polluted weather varies from 0.045 to 0.19 with an altitude from 5 km to 0 km. The mean values of aerosol extinction coefficients decreased exponentially with the increase in altitude, and the variation range of standard deviation decreased gradually. Under non-polluted weather conditions, the mean values of

extinction coefficients changed from 0 to 0.025. With the height rising, the extinction coefficient decreased, and the variation range of standard deviation gradually reduced. The average extinction coefficient of polluted weather is about 10-times that of non-polluted weather.

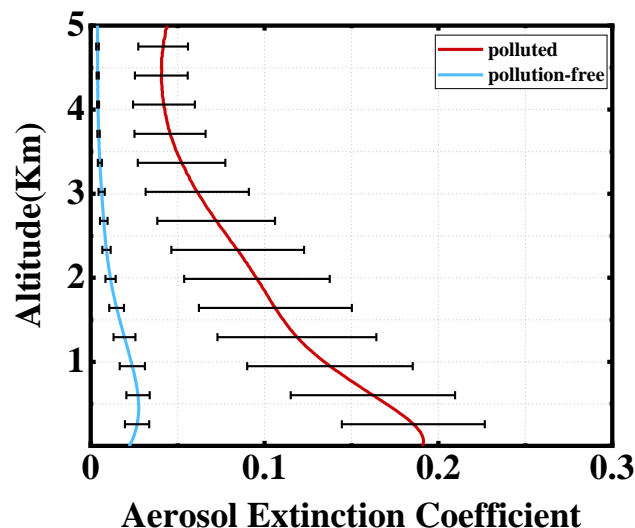


Figure 8. Vertical means and standard deviations map of aerosol 532 nm extinction coefficient based on Lidar for polluted and non-polluted weather at the NYNU site.

Meanwhile, standard deviations of both polluted and non-polluted weather decreased gradually with the increase in altitude (0~5 km), indicating that changes in aerosol concentrations at low altitudes were more significant than that at high altitudes, both in polluted and non-polluted weather. At the same time, the standard deviations in the extinction coefficients for polluted weather, at any altitude, were much larger than those for non-polluted weather. These results indicated that aerosol mass concentrations for polluted weather were higher than that for non-polluted weather at any altitude at the NYNU site. At the same time, the change degree of aerosols in polluted weather was more severe than in non-polluted weather at any altitude.

4. Conclusions

To investigate the vertical distribution of aerosol optical characteristics in Nanyang City, our team developed a ground-based dual-wavelength (532 nm and 355 nm) Lidar system for aerosol studies. The NYNU station in Nanyang City, Henan Province, China, was chosen as the experimental site. The experimental period was from November 2021 to April 2022. The dynamic spatial information and vertical distribution of aerosol optical properties in pollution-free and polluted weathers can be obtained, providing data support and theoretical support for haze prevention and early warning in Nanyang City. The relevant conclusions are as follows:

(1) During the whole experiment period, the vertical distribution of aerosols in non-polluted weather was characterized by a lower altitude (0~2 km), thinner cleaner aerosol layers, and low extinction coefficient values ($\sim 0.03 \text{ km}^{-1}$). The vertical distribution of aerosols in polluted weather was characterized by a thicker aerosol layer (0~4 km) and higher extinction coefficients ($\sim 0.2 \text{ km}^{-1}$).

(2) During the whole experiment period, aerosol extinction coefficient mean values ($0.04\sim 0.19 \text{ km}^{-1}$) at different altitudes (0~5 km) in polluted weather were about 10-times higher than that in non-polluted weather ($0.004\sim 0.02 \text{ km}^{-1}$). At the same time, aerosol extinction coefficient standard deviations ($0.02\sim 0.04$) at different altitudes (0~5 km) in polluted weather were also about 10-times those in non-polluted weather ($0.002\sim 0.006$). These results indicated that aerosol concentrations at different altitudes (0~5 km) were much higher than that during non-pollution days, and aerosol concentration variations were much larger during pollution days than during non-pollution days.

(3) During the whole experiment period, aerosol AOD values of pollution weather (0.4~0.6) were about 10-times those of non-pollution weather (0.05~0.08), which also revealed that aerosol concentrations in polluted weather were much higher than those in non-polluted weather. At the same time, AOD values decreased slightly from 19:00 to 05:00 in polluted and non-polluted weather, indicating that aerosol loadings would decrease slightly at night due to dry depositions.

Author Contributions: Conceptualization, M.Z.; methodology, M.Z. and S.C.; software, S.G. and Y.W.; validation, J.C. and S.C.; formal analysis, M.Z.; investigation, M.Z. and M.B.; resources, M.Z.; data curation, M.Z.; writing—original draft preparation, M.Z.; writing—review and editing, M.B. and M.C.; visualization, M.Z.; supervision, M.Z.; project administration, M.Z.; funding acquisition, M.Z. All authors have read and agreed to the published version of the manuscript.

Funding: This research was funded by the Programs for Science and Technology Development of Henan Province (No. 232102320069); the Nanyang Normal University Scientific Research Project (No. 2020QN033).

Institutional Review Board Statement: Not applicable.

Informed Consent Statement: Not applicable.

Data Availability Statement: Not applicable.

Acknowledgments: We thank the editors for assisting in the linguistic refinement of this manuscript.

Conflicts of Interest: The authors declare no conflict of interest.

References

1. Kaufman, Y.J.; Tanré, D.; Boucher, O. A satellite view of aerosols in the climate system. *Nature* **2002**, *419*, 215–223. [[CrossRef](#)] [[PubMed](#)]
2. Markku, K.; Jenni, K.; Heikki, J.; Katrianne, L.; Manninen, H.E.; Tuomo, N.; Tuukka, P.; Mikko, S.; Siegfried, S.; Pekka, R. Direct observations of atmospheric aerosol nucleation. *Science* **2013**, *339*, 943–946.
3. Qiu, R.; Li, X.; Han, G.; Xiao, J.; Ma, X.; Gong, W. Monitoring drought impacts on crop productivity of the US Midwest with solar-induced fluorescence: GOSIF outperforms GOME-2 SIF and MODIS NDVI, EVI, and NIRv. *Agric. For. Meteorol.* **2022**, *323*, 109038. [[CrossRef](#)]
4. Liu, B.; Ma, X.; Guo, J.; Li, H.; Jin, S.; Ma, Y.; Gong, W. Estimating hub-height wind speed based on a machine learning algorithm: Implications for wind energy assessment. *Atmos. Chem. Phys.* **2023**, *23*, 3181–3193. [[CrossRef](#)]
5. Jacobson, M.Z. Strong radiative heating due to the mixing state of black carbon in atmospheric aerosols. *Nature* **2001**, *409*, 695–697. [[CrossRef](#)] [[PubMed](#)]
6. Cappa, C.D.; Onasch, T.B.; Massoli, P.; Worsnop, D.R.; Bates, T.S.; Cross, E.S.; Davidovits, P.; Hakala, J.; Hayden, K.L.; Jobson, B.T.; et al. Radiative Absorption Enhancements Due to the Mixing State of Atmospheric Black Carbon. *Science* **2012**, *337*, 1078. [[CrossRef](#)]
7. Menon, S.; Hansen, J.; Nazarenko, L.; Luo, Y. Climate Effects of Black Carbon Aerosols in China and India. *Science* **2002**, *297*, 2250–2253. [[CrossRef](#)]
8. Shi, T.; Han, G.; Ma, X.; Mao, H.; Chen, C.; Han, Z.; Pei, Z.; Zhang, H.; Li, S.; Gong, W. Quantifying factory-scale CO₂/CH₄ emission based on mobile measurements and EMISSION-PARTITION model: Cases in China. *J. Environ. Res. Lett.* **2023**, *18*, 034028. [[CrossRef](#)]
9. Zhang, H.; Han, G.; Ma, X.; Chen, W.; Zhang, X.; Liu, J.; Gong, W. Spectral Energy Model-Driven Inversion of XCO₂ in IPDA Lidar Remote Sensing. *IEEE Trans. Geosci. Remote Sens.* **2023**, *61*, 4100609. [[CrossRef](#)]
10. Huang, R.J.; Zhang, Y.; Bozzetti, C.; Ho, K.F.; Cao, J.J.; Han, Y.; Daellenbach, K.R.; Slowik, J.G.; Platt, S.M.; Canonaco, F. High secondary aerosol contribution to particulate pollution during haze events in China. *Nature* **2014**, *514*, 218–222. [[CrossRef](#)]
11. Zhang, Q.; Jiang, X.; Tong, D.; Davis, S.J.; Zhao, H.; Geng, G.; Feng, T.; Zheng, B.; Lu, Z.; Streets, D.G. Transboundary health impacts of transported global air pollution and international trade. *Nature* **2017**, *543*, 705–709. [[CrossRef](#)] [[PubMed](#)]
12. Kaiser, J.; Granmar, M. Mounting Evidence Indicts Fine-Particle Pollution. *Science* **2005**, *307*, 1858–1861. [[CrossRef](#)] [[PubMed](#)]
13. Fu, Q.; Zhuang, G.; Wang, J.; Xu, C.; Huang, K.; Li, J.; Hou, B.; Lu, T.; Streets, D.G. Mechanism of formation of the heaviest pollution episode ever recorded in the Yangtze River Delta, China. *Atmos. Environ.* **2008**, *42*, 2023–2036. [[CrossRef](#)]
14. Tao, M.; Chen, L.; Wang, Z.; Wang, J.; Tao, J.; Wang, X. Did the widespread haze pollution over China increase during the last decade? A satellite view from space. *Environ. Res. Lett.* **2016**, *11*, 054019. [[CrossRef](#)]
15. Qin, Y.; Oduyemi, K. Atmospheric aerosol source identification and estimates of source contributions to air pollution in Dundee, UK. *Atmos. Environ.* **2003**, *37*, 1799–1809. [[CrossRef](#)]
16. Ma, X.; Zhang, H.; Han, G.; Mao, F.; Xu, H.; Shi, T.; Hu, H.; Sun, T.; Gong, W. A Regional Spatiotemporal Downscaling Method for CO₂ Columns. *IEEE Trans. Geosci. Remote Sens.* **2021**, *59*, 8084–8093. [[CrossRef](#)]

17. Che, H.; Xia, X.; Zhu, J.; Li, Z.; Dubovik, O.; Holben, B.; Goloub, P.; Chen, H.; Estelles, V.; Cuevasagulló, E. Column aerosol optical properties and aerosol radiative forcing during a serious haze-fog month over North China Plain in 2013 based on ground-based sunphotometer measurements. *Atmos. Chem. Phys.* **2014**, *14*, 2125–2138. [[CrossRef](#)]
18. Shen, X.J.; Sun, J.Y.; Zhang, X.Y.; Zhang, Y.M.; Zhang, L.; Che, H.C.; Ma, Q.L.; Yu, X.M.; Yue, Y.; Zhang, Y.W. Characterization of submicron aerosols and effect on visibility during a severe haze-fog episode in Yangtze River Delta, China. *Atmos. Environ.* **2015**, *120*, 307–316. [[CrossRef](#)]
19. Zhang, M.; Ma, Y.; Gong, W.; Zhu, Z. Aerosol Optical Properties of a Haze Episode in Wuhan Based on Ground-Based and Satellite Observations. *Atmosphere* **2014**, *5*, 699–719. [[CrossRef](#)]
20. Zhang, M.; Liu, J.; Bilal, M.; Zhang, C.; Gong, W. Aerosol Optical Properties and Contribution to Differentiate Haze and Haze-Free Weather in Wuhan City. *Atmosphere* **2020**, *11*, 322. [[CrossRef](#)]
21. Zhang, X.; Huang, Y.; Zhu, W.; Rao, R. Aerosol characteristics during summer haze episodes from different source regions over the coast city of North China Plain. *J. Quant. Spectrosc. Radiat. Transf.* **2013**, *122*, 180–193. [[CrossRef](#)]
22. Bourgeois, Q.; Ekman, A.M.L.; Krejci, R. Aerosol transport over the Andes from the Amazon Basin to the remote Pacific Ocean: A multiyear CALIOP assessment. *J. Geophys. Res. Atmos.* **2015**, *120*, 8411–8425. [[CrossRef](#)]
23. Mishra, A.K.; Koren, I.; Rudich, Y. Effect of aerosol vertical distribution on aerosol-radiation interaction: A theoretical prospect. *Heliyon* **2015**, *1*, e00036. [[CrossRef](#)]
24. Reddy, K.; Ahammed, Y.N.; Kumar, D.V.P. Effect of cloud reflection on direct aerosol radiative forcing: A modelling study based on lidar observations. *Remote Sens. Lett.* **2014**, *5*, 277–285. [[CrossRef](#)]
25. Chen, C.; Song, X.; Wang, Z.; Chen, Y.; Wang, X.; Bu, Z.; Zhang, X.; Zhuang, Q.; Pan, X.; Li, H.; et al. Calibration Methods of Atmospheric Aerosol Lidar and a Case Study of Haze Process. *Front. Phys.* **2022**, *10*, 942926. [[CrossRef](#)]
26. Winker, D.M.; Pelon, J.R.; McCormick, M.P. The CALIPSO mission: Spaceborne lidar for observation of aerosols and clouds. *Bull. Am. Meteorol. Soc.* **2010**, *91*, 1211–1229. [[CrossRef](#)]
27. Bangia, T.; Kumar, A.; Sagar, R.; Agarwal, P.K.; Singh, S.K. Development of Mie LIDAR system and initial cloud observations over Central Himalayan region. *Sci. Res. Essays* **2011**, *6*, 896–907.
28. Mcgrath-Spangler, E.L.; Scott, D.A. Global seasonal variations of midday planetary boundary layer depth from CALIPSO space-borne LIDAR. *J. Geophys. Res. Atmos.* **2013**, *118*, 1226–1233. [[CrossRef](#)]
29. Zhang, M.; Han, G.; Sun, J.; Gong, W. Two-wavelength depolarization Mie Lidar for tropospheric aerosol measurements. In Proceedings of the IGARSS 2016—2016 IEEE International Geoscience and Remote Sensing Symposium, Beijing, China, 10–15 July 2016; pp. 4051–4054.
30. Huang, J.; Guo, J.; Wang, F.; Liu, Z.; Jeong, M.J.; Yu, H.; Zhang, Z. CALIPSO inferred most probable heights of global dust and smoke layers. *J. Geophys. Res. Atmos.* **2015**, *120*, 5085–5100. [[CrossRef](#)]
31. Mishra, M.K.; Rajeev, K.; Thampi, B.V.; Parameswaran, K.; Nair, A. Micro pulse lidar observations of mineral dust layer in the lower troposphere over the southwest coast of Peninsular India during the Asian summer monsoon season. *J. Atmos. Sol.-Terr. Phys.* **2010**, *72*, 1251–1259. [[CrossRef](#)]
32. Mishra, A.K.; Shibata, T. Climatological aspects of seasonal variation of aerosol vertical distribution over central Indo-Gangetic belt (IGB) inferred by the space-borne lidar CALIOP. *Atmos. Environ.* **2012**, *46*, 365–375. [[CrossRef](#)]
33. Niranjana, K.; Madhavan, B.L.; Sreekanth, V. Micro pulse lidar observation of high altitude aerosol layers at Visakhapatnam located on the east coast of India. *Geophys. Res. Lett.* **2007**, *34*, 340–354. [[CrossRef](#)]
34. Solanki, R.; Singh, N. LIDAR observations of the vertical distribution of aerosols in free troposphere: Comparison with CALIPSO level-2 data over the central Himalayas. *Atmos. Environ.* **2014**, *99*, 227–238. [[CrossRef](#)]
35. Ramanathan, V.; Chung, C.; Kim, D.; Bettge, T.; Buja, L.; Kiehl, J.T.; Washington, W.M.; Fu, Q.; Sikka, D.R.; Wild, M. Atmospheric Brown Clouds: Impacts on South Asian Climate and Hydrological Cycle. *Proc. Natl. Acad. Sci. USA* **2005**, *102*, 5326–5333. [[CrossRef](#)]
36. Nishizawa, T.; Sugimoto, N.; Matsui, I.; Shimizu, A.; Higurashi, A.; Jin, Y. Asian Dust and Aerosol Lidar Observation Network (AD-Net): Strategy and Progress. Presented at the International Laser Radar Conference 2015, New York, NY, USA, 5–10 July 2015.
37. Wang, L.; Gong, W.; Ma, Y.; Hu, B.; Wang, W.; Zhang, M. Analysis of ultraviolet radiation in Central China from observation and estimation. *Energy* **2013**, *59*, 764–774. [[CrossRef](#)]
38. Bucci, S.; Cagnazzo, C.; Cairo, F.; Liberto, L.D.; Fierli, F. Aerosol variability and atmospheric transport in the Himalayan region from CALIOP 2007–2010 observations. *Atmos. Chem. Phys. Discuss.* **2013**, *13*, 15271–15299. [[CrossRef](#)]
39. Sicard, M.; Molero, F.; Guerrero-Rascado, J.L.; Pedros, R.; Exposito, F.J.; Cordoba-Jabonero, C.; Bolarin, J.M.; Comeron, A.; Rocadenbosch, F.; Pujadas, M. Aerosol Lidar Intercomparison in the Framework of SPALINET—The Spanish Lidar Network: Methodology and Results. *IEEE Trans. Geosci. Remote Sens.* **2009**, *47*, 3547–3559. [[CrossRef](#)]
40. Gasmi, K. Measurements of profiles of aerosol/cloud in the lower atmosphere using a lidar system. Presented at the SPIE Remote Sensing 2016, Scotland, UK, 26–29 September 2016.
41. Liu, C.; Chen, Z.; Lv, L.; Liu, W.; Fan, G.; Zhang, T.; Liu, Y.; Dong, Y. Atmospheric Aerosols Detection Research with a Dual Field of View Lidar. *J. Spectrosc.* **2015**, *5*, 459460.
42. Li, B.; Chen, S.; Zhang, Y.; Chen, H.; Guo, P. Fluorescent aerosol observation in the lower atmosphere with an integrated fluorescence-Mie lidar. *J. Quant. Spectrosc. Radiat. Transf.* **2019**, *227*, 211–218. [[CrossRef](#)]

43. Shukla, K.K.; Phanikumar, D.V.; Kumar, K.N.; Kumar, A.; Naja, M.; Sharma, S.; Attada, R. Micro-Pulse Lidar observations of elevated aerosol layers over the Himalayan region—ScienceDirect. *J. Atmos. Sol.-Terr. Phys.* **2021**, *213*, 105526. [[CrossRef](#)]
44. Zhu, J.; Wang, S.; Xu, D.; Liu, D.; Wang, J.; Zhang, S.; Xue, R.; Tang, G.; Zhou, B. Comparative observation of aerosol vertical profiles in urban and suburban areas: Impacts of local and regional transport. *Sci. Total Environ.* **2022**, *805*, 150363. [[CrossRef](#)]
45. Sugimoto, N.; Shimizu, A.; Nishizawa, T.; Matsui, I.; Jin, Y.; Khatri, P.; Irie, H.; Takamura, T.; Aoki, K.; Thana, B. Aerosol characteristics in Phimai, Thailand determined by continuous observation with a polarization sensitive Mie–Raman lidar and a sky radiometer. *Environ. Res. Lett.* **2015**, *10*, 065003. [[CrossRef](#)]
46. Rosati, B.; Herrmann, E.; Bucci, S.; Fierli, F.; Cairo, F.; Gysel, M.; Tillmann, R.; Gr, J.; Gobbi, G.P.; Di Liberto, L.; et al. Studying the vertical aerosol extinction coefficient by comparing in situ airborne data and elastic backscatter lidar. *Atmos. Chem. Phys.* **2016**, *16*, 4539–4554. [[CrossRef](#)]
47. Navas-Guzmán, F.; Martucci, G.; Coen, M.C.; Granados-Muoz, M.J.; Haefele, A. Characterization of aerosol hygroscopicity using Raman lidar measurements at the EARLINET station of Payerne. *Atmos. Chem. Phys.* **2019**, *19*, 11651–11668. [[CrossRef](#)]
48. Volker, M.; Volker, F.; Aldo, A.; Ioan, B.; Dimitris, B.; Jens, B.S.; Anatoly, C.; Georgius, C.; Adolfo, C.; Arnaud, D. Aerosol lidar intercomparison in the framework of the EARLINET project. 1. Instruments. *Appl. Opt.* **2004**, *43*, 961–976.
49. Zhang, M.; Wu, D.; Su, B.; Bilal, M.; Li, B.L. Spatio-Temporal Characteristics of PM 2.5, PM 10, and AOD over Canal Head Taocha Station, Henan Province. *Remote Sens.* **2020**, *12*, 3432. [[CrossRef](#)]
50. Collis, R.T.H. Lidar: A new atmospheric probe. *Q. J. R. Meteorol. Soc.* **1966**, *92*, 220–230. [[CrossRef](#)]
51. Klett, J.D. Stable analytical inversion solution for processing lidar returns. *Appl. Opt.* **1981**, *20*, 211–220. [[CrossRef](#)]
52. Fernald, F.G. Analysis of atmospheric lidar observations: Some comments. *Appl. Opt.* **1984**, *23*, 652–653. [[CrossRef](#)]
53. Omar, A.H.; Winker, D.M.; Kittaka, C.; Vaughan, M.A.; Liu, Z.; Hu, Y.; Trepte, C.R.; Rogers, R.R.; Ferrare, R.A.; Lee, K.P. The CALIPSO Automated Aerosol Classification and Lidar Ratio Selection Algorithm. *J. Atmos. Ocean. Technol.* **2009**, *26*, 1994–2014. [[CrossRef](#)]
54. Kim, M.H.; Omar, A.H.; Tackett, J.L.; Vaughan, M.A.; Magill, B.E. The CALIPSO Version 4 Automated Aerosol Classification and Lidar Ratio Selection Algorithm. *Atmos. Meas. Tech.* **2018**, *11*, 6107–6135. [[CrossRef](#)] [[PubMed](#)]
55. Tao, Z.; Liu, Z.; Dong, W.; McCormick, M.P.; Jia, S. Determination of aerosol extinction-to-backscatter ratios from simultaneous ground-based and spaceborne lidar measurements. *Opt. Lett.* **2008**, *33*, 2986–2988. [[CrossRef](#)] [[PubMed](#)]
56. Müller, D.; Ansmann, A.; Mattis, I.; Tesche, M.; Wandinger, U.; Althausen, D.; Pisani, G. Aerosol-type-dependent lidar ratios observed with Raman lidar. *J. Geophys. Res.* **2007**, *112*, D16202. [[CrossRef](#)]
57. Chen, Y.; Schleicher, N.; Fricker, M.; Cen, K.; Liu, X.L.; Kaminski, U.; Yu, Y.; Wu, X.F.; Norra, S.J.E.P. Long-term variation of black carbon and PM_{2.5} in Beijing, China with respect to meteorological conditions and governmental measures. *Environ. Pollut.* **2016**, *212*, 269–278. [[CrossRef](#)]

Disclaimer/Publisher’s Note: The statements, opinions and data contained in all publications are solely those of the individual author(s) and contributor(s) and not of MDPI and/or the editor(s). MDPI and/or the editor(s) disclaim responsibility for any injury to people or property resulting from any ideas, methods, instructions or products referred to in the content.